Physics of the Earth and Planetary Interiors 375 (2026) 107556

Contents lists available at ScienceDirect

Physics of the Earth and Planetary Interiors

journal homepage: www.elsevier.com/locate/pepi

Illuminating mantle structures at Western Galápagos using seismic interferometry by autocorrelation with body waves

Eugenia Boero [a,b,*], José Augusto Casas [a,b,c], Gabriela Alejandra Badi [a], Deyan Draganov [d]

[a] Centro de Investigaciones Geofísicas (CIGEOF), Facultad de Ciencias Astronómicas y Geofísicas, Universidad Nacional de La Plata, Argentina
[b] Consejo Nacional de Investigaciones Científicas y Técnicas (CONICET), Argentina
[c] Observatorio Argentino de Vigilancia Volcánica, Servicio Geológico Minero Argentino (OAVV-SEGEMAR), Argentina
[d] Delft University of Technology (TU Delft), The Netherlands

ARTICLE INFO

Dataset link: Seismic waveform data from the SIGNET network (Original data)

Keywords:
Galápagos
Seismic interferometry
Mantle discontinuities
Mantle plume

ABSTRACT

The Galápagos archipelago is one of the regions with the highest rates of eruption and surface magma emission in the world. Knowledge about the subsurface structure is fundamental for a better understanding of the dynamics of the magmatic systems in the area. However, the details of the internal architecture beneath the archipelago remain poorly constrained at both shallow and deep levels. To shed light on these, we apply seismic interferometry by autocorrelation to records of earthquakes with epicentral distances greater than 30°, obtained from 18 broadband stations deployed around two volcanoes (Cerro Azul and Sierra Negra) located in Western Galápagos, which is characterized by the highest volcanic activity of the archipelago. The methodology we apply results in the identification of the main mantle discontinuities at a wide range of depths with high resolution. We combine the individual results from all stations to construct a representative depth model for the entire region down to a depth of 800 km. Our results reveal coherent reflectivity patterns consistent with previously identified mantle structures and define the extent and location of the Galápagos mantle plume. These findings provide new insights into the mantle structure beneath the archipelago and can be used to improve our understanding of plume processes driving volcanism and its surface expression in the region.

1. Introduction

State-of-the-art volcanology research confronts the challenge of illuminating the internal structure of volcanic systems, encompassing regions of magma generation to emission vents on the volcanic edifice. These insights are critical to understanding volcano dynamics, accurately inferring behavioral evolution, and developing effective alert systems to mitigate associated risks (Sigurdsson et al., 2015).

About 23 million years ago, an east–west rifting process began between the Cocos and the Nazca plates, leading to the formation of the Galápagos Spreading Center (Hey, 1977). This tectonic setting was further influenced by the presence of a mantle plume, currently located about 1000 km west of the coast of Ecuador, which gave rise to the Galápagos hotspot (Simkin, 1984). This system, together with the Nazca Plate's movements over the Galápagos hotspot, formed the Galápagos archipelago (Fig. 1(a))- a group of volcanic islands located in the Pacific between 100 and 300 km south of this spreading center (Geist et al., 2008). This area constitutes one of the most volcanically active regions in the world (Geist et al., 2014; Simkin and Howard, 1970). The youngest and most active volcanoes of the archipelago are located in its western sector (Harpp and Geist, 2018; Siebert et al., 2010). Among these are the Sierra Negra and Cerro Azul volcanoes, which are located in the southern part of Isabela Island, the study area of this work (Fig. 1(b)).

Volcanic activity in the Galápagos is influenced by the mantle plume, as its ascent and partial melting beneath the archipelago supply magma to active volcanoes, such as Sierra Negra and Cerro Azul (Geist et al., 1988). Montelli et al. (2004), using finite-frequency tomography, imaged the Galápagos plume in the upper mantle, suggesting an origin at a depth of less than 1000 km, with a radius of 300 km centered at 0° latitude and 92° W longitude. Villagómez et al. (2014) proposed that the mantle plume is deflected or bent beneath the archipelago on its way toward the Galápagos Spreading Center, and that this bending occurs at depths greater than 150 km; their seismic-tomography results indicate that the plume is centered at ~250 km depth beneath the archipelago, with its deeper portion located south of Isabela Island starting at depths greater than 150 km. Based on receiver-function

* Corresponding author at: Centro de Investigaciones Geofísicas (CIGEOF), Facultad de Ciencias Astronómicas y Geofísicas, Universidad Nacional de La Plata, Argentina.
E-mail address: eboero@fcaglp.unlp.edu.ar (E. Boero).

https://doi.org/10.1016/j.pepi.2026.107556
Received 7 August 2025; Received in revised form 14 January 2026; Accepted 12 April 2026
Available online 28 April 2026

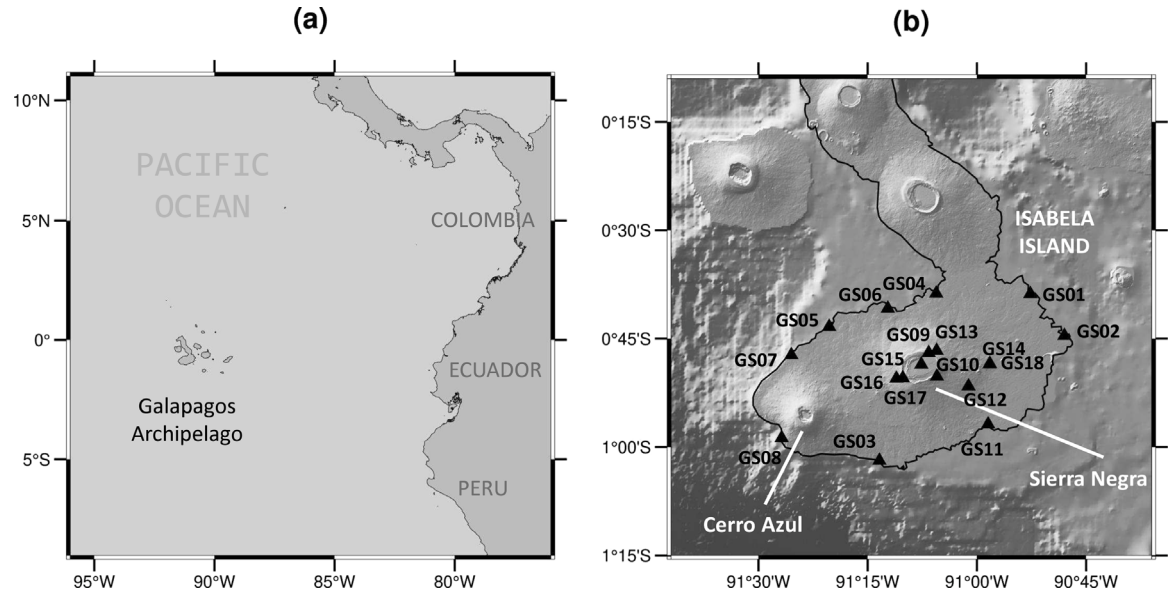

Fig. 1. (a) Location of the Galápagos Archipelago in relation to Western South America. (b) Topographic map centered on the southern part of Isabela Island, showing the station distribution (solid triangles) around the Sierra Negra and Cerro Azul volcanoes.

imaging, Rychert et al. (2014) observed an increase in velocity at 130 140 km depth, indicating that this is probably related to the onset of the molten zone; they also identified this discontinuity at depths greater than 145 km in the southern part of the archipelago.

Rychert et al. (2014) indicated a depth of 75 ± 12 km for the lithosphere asthenosphere boundary (LAB) in the Galápagos region, presenting a depth of 82 km below Isabela Island. Through receiver-functions analyses, Byrnes et al. (2015) inferred the location of the "discontinuity G" at 91±8 km depth below Southeastern Galápagos and 72±5 km depth in its surroundings. They argued that this discontinuity corresponds to the base of a fully dehydrated mantle, where upwelling and decompression melting occur. They concluded that this discontinuity is not relevant for the LAB, as it does not present the expected mechanical properties.

At the global scale, several studies have detected a seismic discontinuity at a depth of approximately 300 km beneath island arcs (Leven, 1985; Wajeman, 1988; Williams and Revenaugh, 2005). This feature has been associated with geochemical heterogeneity in the mantle and a residue of ancient subduction within the upper mantle. In the Galápagos region, it was observed through analyses of SS phases between 290 and 330 km depth (Deuss and Woodhouse, 2002).

The 410 and 660 km discontinuities are globally recognized, defining the boundaries of the transition zone (TZ) (Frost, 2008). Using precursor stacking techniques, both discontinuities are clearly visible in stacked images of global datasets, indicating that they do not vary significantly between regions (Shearer, 1990). However, the 660 km discontinuity exhibits a more complex structure, displaying a significantly varying character and sometimes presenting double peaks at depths of 650 750 km (Deuss, 2009).

Within the TZ, a secondary seismic discontinuity, with an amplitude roughly half that of the 410 km discontinuity, is generally observed around 520 km depth, although it exhibits a more complex structure and its presence is spatially variable (Deuss, 2009; Shearer, 1990). Based on analyses of SS phase coherency, Deuss and Woodhouse (2001) reported a discontinuity at approximately 520 km depth in many regions; however, in several areas, including the mid-Pacific, which encompasses the Galápagos, they identified two distinct discontinuities at about 500 and 560 km depth. They associated these two discontinuities with a splitting effect of the 520 km discontinuity, originating from a wadsleyite-to-ringwoodite phase transition, a compositional transition that is absent from most reference models (Frost, 2008).

Based on experimental petrology, Ringwood (1968) proposed the existence of a discontinuity at the base of the TZ, attributed to the accumulation of ancient subducted oceanic crust. Shen et al. (2014), using global stacks of receiver functions, identified a discontinuity near 600 km depth beneath both continental and island stations, supporting the idea that it may represent a global feature.

Many details about the archipelago's subsurface remain to be discerned, including the precise location and dimensions of the mantle plume beneath it, as well as the complex mantle structure that influences the region's volcanic activity and tectonic processes. The objective of our work is to provide evidence on the location of mantle structures beneath the Sierra Negra and Cerro Azul volcanoes. To this end, we apply seismic interferometry (SI), a method that allows for the extraction of subsurface information from complex or random wavefields, providing valuable insights that can also enhance conventional seismic approaches (e.g., Brenguier et al., 2008; Draganov et al., 2007; Sens-Schönfelder and Wegler, 2006). Specifically, by applying SI by autocorrelation to distant earthquakes, we retrieve body-wave reflections and illuminate the structure beneath selected stations in the vertical direction, allowing for the identification of seismic discontinuities (Nishitsuji et al., 2016; Pham and Tkalčić, 2017; Ruigrok et al., 2010; Ruigrok and Wapenaar, 2012; Sun and Kennett, 2016; Tauzin et al., 2019). For this purpose, we use seismic events recorded at 18 broadband seismological stations deployed around Sierra Negra and Cerro Azul volcanoes between August 2009 and June 2011 (Fig. 1(b)). Results from individual stations are then combined to obtain a representative subsurface structure for the entire region. This is achieved using a stacking technique that improves statistical robustness, enhances coherent seismic signals, and suppresses noise and station-specific effects. We provide precise measurements of the locations of subsurface structures in the mantle, confirming the presence of previously identified features and refining the geological model for southern Isabela Island in the Western Galápagos.

2. Methodology

SI exploits the interference patterns in the propagation of seismic energy to retrieve relevant information about the propagation medium. It uses recordings from one or multiple stations, from artificial or natural seismic sources. By reorganizing a wavefield recorded at different stations, SI retrieves new seismograms in which one of the sensors,

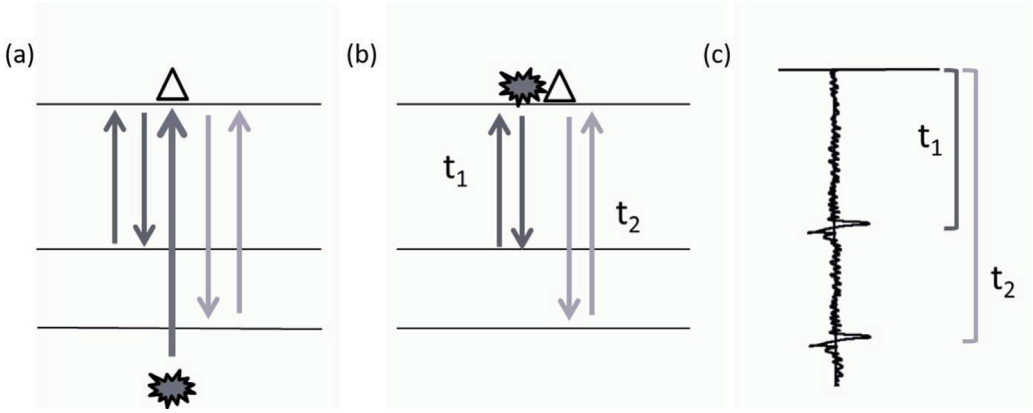

Fig. 2. Seismic interferometry by autocorrelation applied to vertically incident seismic energy. (a) A subsurface source emits seismic waves toward the surface, which are reflected at various interfaces and recorded by a receiver. (b) Result of applying seismic interferometry by autocorrelation: a virtual source is located at the surface, and only the reflected energy is retrieved. The variables t_1 and t_2 represent the two-way travel times to the reflectors. (c) Seismogram at the receiver location retrieved from the autocorrelation process, showing the vertical reflectivity response.

referred to as a virtual source, acts as the source of energy for the other stations. Then, SI could provide precise estimates of the medium's impulse response, i.e., the empirical Green's function, between every virtual source station pair (Wapenaar et al., 2010). This method has been successfully applied to global phases, teleseismic phases, microseisms, and ambient seismic noise to image the interior of the Earth at various scales (Boullenger et al., 2014; Casas et al., 2020; Draganov et al., 2007; Gorbatov et al., 2013; Kim et al., 2017; Nishitsuji et al., 2016; Oren and Nowack, 2017; Ruigrok and Wapenaar, 2012).

SI by autocorrelation is an SI technique with active or passive sources that does not require prior knowledge about the propagation medium or sources to obtain information about subsurface structures. Claerbout (1968) laid a basis upon which SI by autocorrelation was developed. He proved that the autocorrelation of the transmission response of a plane wave through a horizontally stratified medium, recorded at the surface, allows retrieving the reflection response of a virtual source co-located with the recording station.

The mathematical formulation of SI by autocorrelation for general inhomogeneous medium was developed by Wapenaar and Fokkema (2006). They obtained the relation:

$$\sum_i \left[T(r_0,-t) * s_i(-t) * T(r_0,t) * s_i(t)\right] \otimes [s(-t) * s(t)]_i \approx -R(r_0,-t) + \delta(t) - R(r_0,t), \quad (1)$$

where $s_i(t)$ denotes the time function of the source i; $[s(-t) * s(t)]_i$ refers to the autocorrelated source time function; the transmitted wavefield recorded at the station and the reflection response observed at the position r_0 are represented by $T(r_0,t)$ and $R(r_0,t)$, respectively; $\delta(t)$ denotes the Dirac delta function; and symbols $*$ and $\otimes$ denote convolution and deconvolution operators, respectively. This equation establishes that the reflection response $R(r_0,t)$ can be retrieved by autocorrelating the transmitted wavefield $T(r_0,t)$. Even though the theory assumes lossless media, this formulation does not preclude its application to media with anelastic losses - theoretical analyses have demonstrated the robustness of this technique in addressing such limitations (Vasconcelos et al., 2009). Furthermore, numerous studies have confirmed the adaptability of SI by autocorrelation to seismic data recorded in complex environments such as volcanic areas (Casas et al., 2019, 2020; Hassing et al., 2023; Heath et al., 2018; Nacif et al., 2024; Polychronopoulou et al., 2019).

Fig. 2 illustrates the basic principle of SI by autocorrelation assuming a 1D medium. A source in the subsurface emits energy vertically toward the surface, where it is reflected back into the subsurface (Fig. 2(a)). The seismogram at a station located at the surface will then contain the arrival of direct waves followed by energy that is multiply reflected between the surface and several subsurface discontinuities along their vertical trajectories. By applying SI by autocorrelation to the receiver's record, the multiply reflected arrivals are isolated, while the incoherent noise is attenuated. Subsequently, the two-way travel times of the seismic energy to the subsurface discontinuities are retrieved. Therefore, SI by autocorrelation allows for the estimation of the two-way travel time of discontinuities, providing information about the subsurface architecture of the analyzed area.

3. Data

We apply SI by autocorrelation to data recorded at 18 broadband seismological stations (GS01 - GS18) of the temporary Sierra Negra Integrated Geophysical Network (SIGNET). These stations were installed in the southern part of Isabela Island between August 2009 and June 2011, covering an elliptical area of approximately 75 km × 45 km, including the Sierra Negra and Cerro Azul volcanoes (Fig. 1(b)). The dataset, freely available from the Incorporated Research Institutions for Seismology (IRIS) database, consists of velocity recordings sampled at 40 Hz (GS01 GS13) or 50 Hz (GS14 GS18).

The P-wave coda recorded in the vertical component is an accurate measurement of the transmission response for the P-wave energy propagating along the vertical direction (Wapenaar et al., 2010). Through SI, we use the transmission response to retrieve the reflection energy along the vertical component. The application of SI by autocorrelation, when P-wave energy is used, requires a (sub)vertical propagation of the seismic energy in the subsurface. In this case, the seismograms recorded at a station located on the surface will present the arrival of direct waves followed by the arrival of seismic energy reflected and transmitted multiple times between the surface and the subsurface discontinuities (i.e., coda). To ensure that the P-wave energy arrives at the station subvertically, we impose a constraint on the ray parameter of the direct P wave. For steep propagation angles (below 20°), the ray parameter must be < 0.08 s/km (Kennett et al., 1995). Given this condition, we select only events with epicentral distances greater than 30° from each station, ensuring a predominantly vertical to subvertical incidence of the seismic energy; an upper epicentral-distance limit is not required.

For data download, we use the PyWEED software (IRIS, 2015). We download waveforms from earthquakes with magnitude $M_w > 6$ and epicentral distances greater than 30° that occurred during the recording period for each SIGNET station. Based on the previously mentioned criteria, we only used their vertical component records.

Table 1
Number of events used for the application of SI by autocorrelation at each station.

Station	Number of events
GS01	238
GS02	259
GS03	120
GS04	64
GS05	259
GS06	259
GS07	262
GS08	82
GS09	253
GS10	261
GS11	74
GS12	255
GS13	250
GS14	83
GS15	197
GS16	76
GS17	80
GS18	69

4. Application and results

We analyze the downloaded records in two stages: pre-processing and processing. This division allows for a clear distinction between the preparation of the seismic records such as cleaning, filtering, and windowing and the application of a variation of SI to obtain the subsurface reflection response.

4.1. Pre-processing

The Galápagos Archipelago is characterized by active volcanism, plate interactions, and strong lateral heterogeneity, which introduce significant spatio-temporal variability in seismic records and commonly result in low signal-to-noise ratio (SNR). Therefore, after data download, we apply data quality control to exclude traces affected by high-energy coherent noise, and perform frequency filtering to enhance their SNR. Subsequent processing steps, including stacking, further improve signal coherence and attenuate residual incoherent noise.

The quality control is designed to avoid recordings with overlapping seismic events that may introduce spurious artefacts in the autocorrelation. It is implemented in two stages. First, we ensure that the selected time windows predominantly contain P-wave coda energy, while excluding S-wave arrivals, which behave as coherent noise and may introduce cross-terms in the autocorrelation results. To address this, we discard from our catalog the second of two seismic events that occurred so closely in time that the arrival of the S-wave energy from the first overlapped with the P-wave coda of the second. Thus, we avoid correlations between S-wave energy from the first event and P-wave energy from the second. The second step focuses on evaluating the waveform and spectral content of each record individually. This criterion is designed to avoid the presence of local events in the records, as these do not necessarily arrive vertically at the stations. Table 1 lists the number of selected events for each station. As an example, Fig. 3 illustrates ten of the selected events recorded at station GS17 (see Table S1 in Supplementary Material for additional information on the corresponding source parameters).

We then filter the selected records in the frequency range of [0.5, 1] Hz (see Fig. 4(a) and (b)). Within this range, the energy of the P-wave exceeds that of the noise (see Fig. A.1 in Appendix A showing a representative example of the amplitude spectrum of signal and noise intervals). Based on this selected frequency range, we decimate the records to 5 samples per second.

Finally, we extract the useful P-wave coda from the records of each station. To avoid coherent artefacts due to crosstalk between P- and S-wave arrivals in the autocorrelation, the P-wave coda window should be limited to the S-wave arrival. We estimate the theoretical arrival times of the direct P- and S-waves using the global velocity model AK135 (Kennett et al., 1995), along with the locations of the seismic events and the stations. Due to variations in source distances, the lengths of the P-wave codas differ for a given station (see example in Fig. 3). To ensure a uniform contribution in time from all sources, we select the first 200 s of each trace, as this interval includes contributions from all events and it is sufficiently long to explore the mantle depths (Fig. 4(c)).

4.2. Processing

For each event recorded at every station, we compute the normalized autocorrelation of the P-wave coda. This normalization ensures equal energy contribution of each event. Due to the inherent symmetry of autocorrelations, only the causal part is considered for further analysis (Fig. 4(d)). Then, we apply linear stacking individually to the autocorrelation functions obtained for the events of each station (Fig. 4(e)). This retrieves a new individual sequence with reduced signal variability and higher quality (i.e., higher SNR) for each station (see Appendix B for an analysis of the stability and robustness of the resulting single-station linear stacks). We did not apply an explicit source deconvolution to the autocorrelations, as source-related contributions are expected to be largely reduced by the relatively narrow frequency band used, and the subsequent stacking procedure further enhances the structural response while attenuating source and noise effects (Tauzin et al., 2019).

Given the relatively small area enclosed by the stations and the frequencies used in the processing, we expect the information contributed by each station to remain consistent and not differ significantly for deeper structures (i.e., at depths below the Moho). Thus, we combine the information from the stations to obtain a representative subsurface structure for the entire region. To do so, we apply phase-weighted stacking (PWS) to the individual results. The application of both linear stacking and PWS at different stages of processing is known as two-stage stacking (Ventosa and Schimmel, 2017). This approach consists of first improving the SNR through linear stacking, followed by the application of PWS to the resulting signals. This occurs because PWS is more effective when stacking fewer high-quality sequences, rather than a larger number of low-quality ones, even when the linear stacks of those traces are identical. Therefore, for datasets with a large number of low-SNR traces, a two-stage stacking approach is recommended.

As there are differences in the number of events per station, we normalize the linear stacks before combining them. This prevents stations with more events from exerting greater influence, ensuring that all stations contribute equally to the final combined stack. The results of the pre-processing and processing steps for each individual station (i.e., the normalized linear stacks) are shown in Fig. 5(a). After normalization, we combine the traces from all stations (Fig. 5(b)). A dedicated single-station sensitivity analysis Appendix B shows that the main features are consistently observed across individual stations, supporting the stability of the resulting subsurface response. Nevertheless, some variability remains at the single-station level, reflecting the presence of local noise that affects the clarity of certain features. As this noise is largely incoherent across stations, the application of PWS is particularly appropriate. The differences between the PWS result and the individual linear stacks therefore reflect the phase-coherence-based nature of the PWS method, which prioritizes phase coherence over amplitude. We employ PWS in both the time and frequency domains using the S-transform, which enhances coherent signals while strongly attenuating incoherent noise, improving signal clarity and accelerating convergence compared to traditional stacking methods (Ventosa and Schimmel, 2017; Yang et al., 2022). This results in a representative signal that emphasizes features coherently detected across the station network.

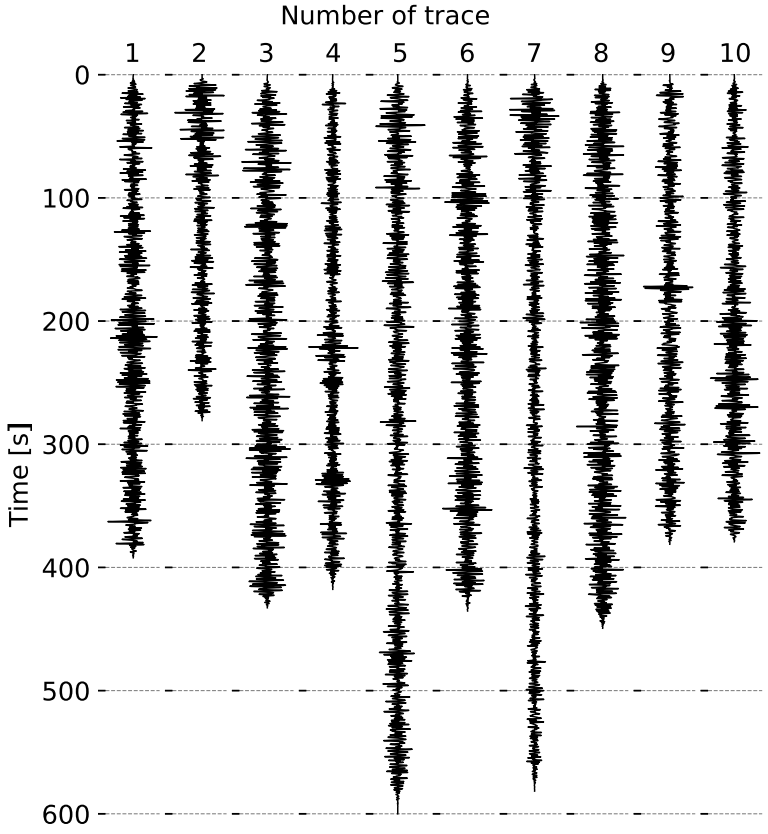

Fig. 3. Traces corresponding to the P-wave codas of the first 10 selected events (chronologically ordered) used for station GS17.

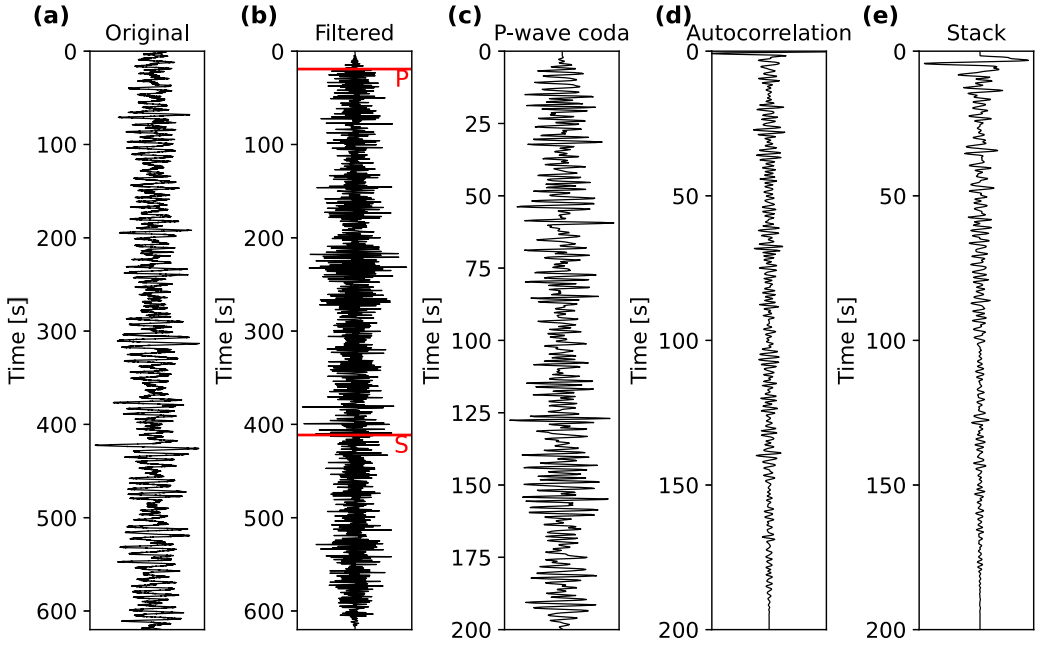

Fig. 4. Pre-processing and processing steps applied to data recorded at each station, illustrated using station GS17 as an example. Panels (a) (d) show the effect of the applied methodology on an arbitrarily chosen seismic event recorded by this station, while panel (e) shows the result obtained using all selected events. (a) Raw trace of a selected event, showing a time window from 20 s before to 600 s after the P-wave arrival. (b) Same trace after frequency filtering with the estimated P- and S-wave arrival times indicated in red. (c) Selected P-wave coda (first 200 s) of the event. (d) Causal part of the autocorrelation of the P-wave coda. (e) Linear stack of all selected events.

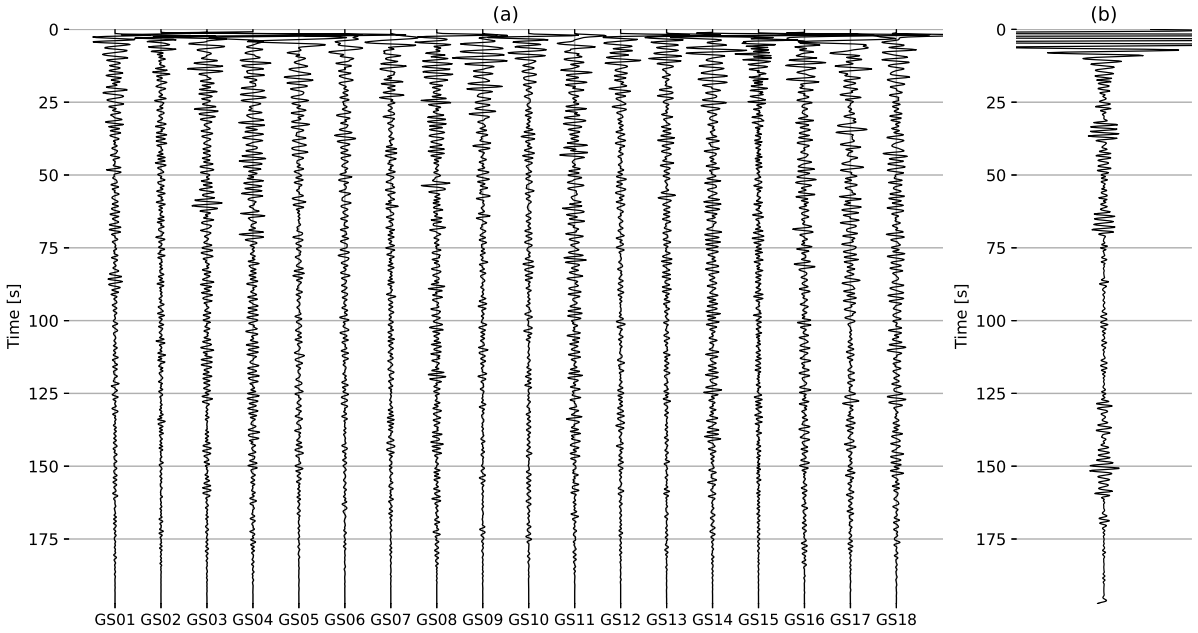

Fig. 5. (a) Normalized results for each station and (b) their combination using the PWS algorithm.

4.3. Results

By performing autocorrelation, the new records and their PWS exhibit vertical reflections where the observed propagation time represents the two-way travel time of the arrivals (Fig. 6(a)). Hence, we convert the resulting two-way-time stack into depth in order to properly interpret the obtained information (Fig. 6(b)). To do so, a velocity model must be adopted. For depths up to 43 km, we use a model applied by the Instituto GeofÃsico de la Escuela PolitÃ©cnica Nacional (IGEPN) for routine monitoring of Sierra Negra volcano (Hidalgo et al., 2023). For greater depths, we utilize the global model AK-135 (Kennett et al., 1995).

As a final processing step, we compute the envelope of the PWS signal using the Hilbert transform (Fig. 6(c)). The peaks of this envelope are automatically identified and are tentatively associated with reflections from major subsurface discontinuities, providing an objective way to indicate their locations.

5. Interpretation and discussion

For the interpretation of the results, we analyze the dominant amplitudes in the final obtained trace (Fig. 6(c)). Specifically, local maxima are distinguished along the envelope of the resulting signal, which are relevant to the main subsurface discontinuities. Our results show P-wave energy reflected and transmitted multiple times at the surface and subsurface discontinuities. Converted waves (e.g., from P to S) could also contribute to the correlation results; however, when vertical components are correlated, the arrivals of converted S-wave energy are expected to attenuate at zero offset (Casas et al., 2020; Delph et al., 2019). This ensures that the observed amplitudes are primarily related to vertically propagating P-waves. Therefore, the observed dominant amplitudes correspond to the subsurface discontinuities where this energy was reflected.

The amplitudes of the local maxima associated with the discontinuities cannot be directly interpreted due to three factors. First, we apply an SI representation that required simplifications, making the absolute amplitudes, and even relative amplitudes in a given autocorrelation function, unreliable (Wapenaar and Fokkema, 2006). Second, the characteristics of the utilized PWS method impose certain limitations; while PWS improves the SNR, it comes at the cost of potential signal distortion due to varying coherence across its time and frequency components (Ventosa and Schimmel, 2017). Third, combining results from different stations introduces additional complexities; although the stations are relatively closely spaced, stacking individual results each representing the vertical component recorded at a specific station complicates the interpretation of the amplitudes. This is because a larger amplitude at a given depth may indicate a stronger impedance contrast in the medium but could also arise from a discontinuity being detected by all stations, without necessarily implying a significant impedance contrast. Nevertheless, despite these limitations, the identification of local maxima remains a robust approach, as their consistent presence and coherent depth across stations provide a reliable indicator of subsurface discontinuities, regardless of the amplitude variability.

Based on the identified local maxima and the comparison of these distinguished features with previous studies, we propose a structural depth model for Western Galápagos. This model is shown in Fig. 7, overlaid on the resulting trace. The uncertainty of the results is influenced by several factors, including the selected frequency band, stacking robustness, inter-station variability, and the adopted velocity model. We evaluate the sensitivity to each of these factors and find that none of them significantly affects the interpretations. First, although the use of a broader frequency band could, in principle, improve the vertical resolution, it would also introduce seismic energy not directly related to seismic events, thereby increasing noise and uncertainty Appendix A. Second, the robustness of the linear stacking procedure is assessed through a dedicated sensitivity test Appendix B. This test indicates that the main identified features are stable and are not controlled by a limited subset of events. Third, inter-station variability is not expected to significantly influence the results at the depths of interest (i.e., below the Moho), where the obtained response is dominated by coherent, large-scale structures detected across all stations, as enhanced by the PWS procedure. Finally, a sensitivity test based on perturbations of the adopted velocity model yields consistent depth estimates Appendix C, indicating that the depth estimates remain stable under reasonable model variations. The remaining uncertainty in the selection of a representative depth within the range is defined by the pulse width of the signal. The pulse width corresponds to the depth interval over which the signal exceeds half of its maximum

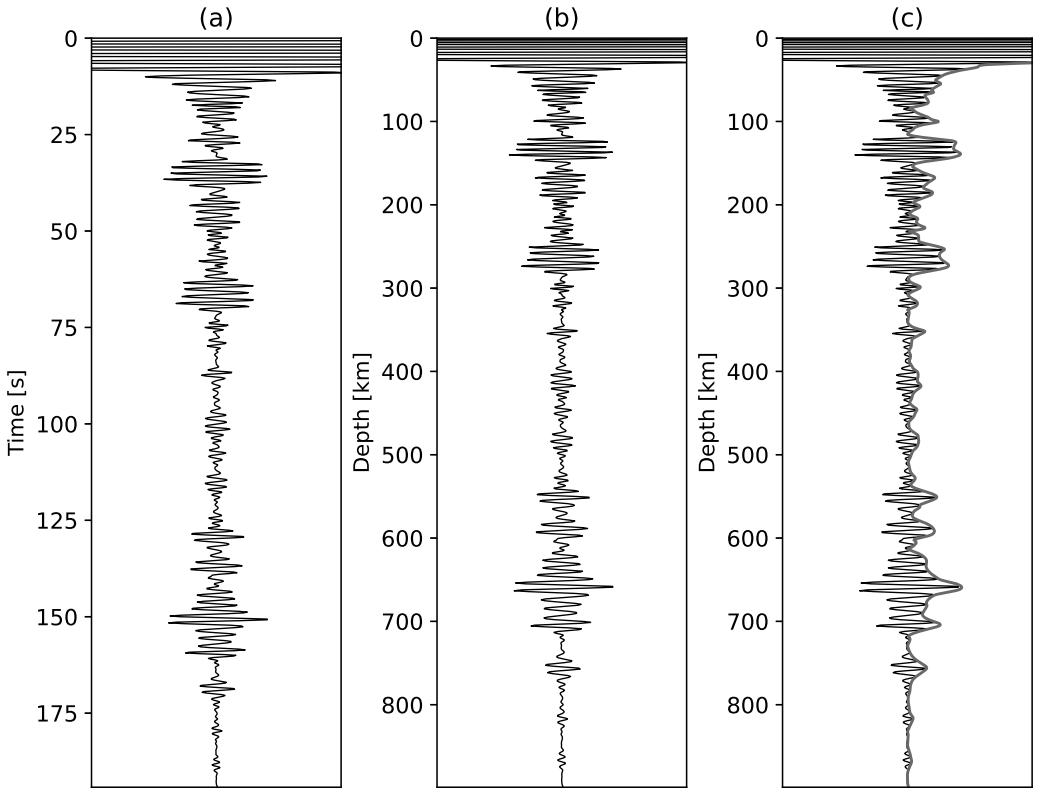

Fig. 6. (a) PWS in the time domain. (b) PWS in the depth domain. (c) PWS in the depth domain with the corresponding signal envelope.

amplitude. In our case, this uncertainty is bounded by an upper limit of approximately 18.25 km, supporting the high resolution of our depth estimates within this interval.

Fig. 7 shows all identified discontinuities on the left and the conceptual layered model on the right. The horizontal bands highlight features interpreted as subsurface reflectors, with their widths corresponding to the associated pulse, thereby defining the resolution of each identified discontinuity. The dark-gray bands indicate clearly distinguishable discontinuities, while the light-gray bands represent features reported in previous studies that appear less prominently in our results. Several factors may contribute to this reduced clarity, including: (i) a genuinely low impedance contrast across the discontinuity, producing weak reflected energy; (ii) a moderate impedance contrast combined with a sufficiently strong dip or curvature of the discontinuity, such that reflected energy is not directed back toward the surface stations; (iii) a gradual transition between subsurface layers, generating multiple closely spaced reflections rather than a single coherent interface; and (iv) a structurally complex discontinuity, in which lateral heterogeneity reduces coherence and hinders effective stacking across stations. Future refinements could include the incorporation of local seismic events with near-vertical incidence or the implementation of criteria to identify and exclude the noisiest correlation functions prior to stacking. These complementary strategies may help enhance the coherence of the resulting signal and potentially improve the identification of subtle maxima.

The shallowest marked discontinuity in Fig. 7 is the LAB, which is expected to be present but does not appear distinctly in our results. Based on the work of Rychert et al. (2014), this discontinuity is located at a depth of 82 km in the southern part of Isabela Island, although the average depth reported for the entire region is 75 ± 12 km. Even though there is no evident variation in relative amplitudes around this depth range, the signal exhibits a higher dominant frequency at the 65.1 ± 1 km pulse, while at shallower and deeper levels the dominant frequency appears lower. Studies of other oceanic hotspots, such as Hawaii, show that thermal interaction with the mantle plume produces a thinner lithosphere, resulting in the LAB being located typically around $50-60$ km depth (Li et al., 2004). Therefore, based on previous knowlege and the shift in dominant frequency observed at this depth, we associate the pulse located at 65.1 ± 1 km with the LAB.

Within the upper mantle, we indicate the shallowest discontinuity at a depth of 100.5 ± 5.2 km. Based on the work of Byrnes et al. (2015) for the Galápagos region, this discontinuity is attributed to a mineralogical transition and/or the accumulation of partial melt, associated with the presence of the mantle plume, reflecting a local phenomenon. In addition, Byrnes et al. (2015) support the interpretation of a lithosphere thinned over the plume, distinguishing this feature from the LAB.

Our results show the presence of two other very pronounced discontinuities within the upper mantle. The first is associated with two pulses at 125.5 ± 1.9 km and 139.3 ± 12.7 km, with very similar amplitudes and frequency behavior. The overlap and continuity of these depth ranges indicate that the discontinuity extends from 123.6 to 152.0 km, and is therefore represented by a mean depth of 137.8 ± 14.2 km. The second discontinuity is also associated with two pulses at depths of 253.4 ± 2.0 km and 273.0 ± 14.9 km beneath the analyzed region. Following the same criteria, this corresponds to a single feature at 269.7 ± 18.3 km. In line with the plume geometry proposed by Villagómez et al. (2014), we interpret these features as the upper and lower boundaries of a mantle plume structure, based on their depth and spatial extent. According to our observations, the plume beneath this region of the archipelago has a vertical extent of approximately 130 km. Although variations in amplitude and signal behavior are observed within the plume, we do not associate any of them with a specific discontinuity. Instead, we interpret these variations as potential heterogeneities within the plume itself, possibly related to variations on the percentage of melting or mineralogical changes.

We identify another discontinuity in the upper mantle at 351.9 ± 4.2 km depth. We associate this feature with the compositional transition estimated to occur around 300 km beneath volcanic arcs (Williams and Revenaugh, 2005). Smaller peaks are also observed around 298.7

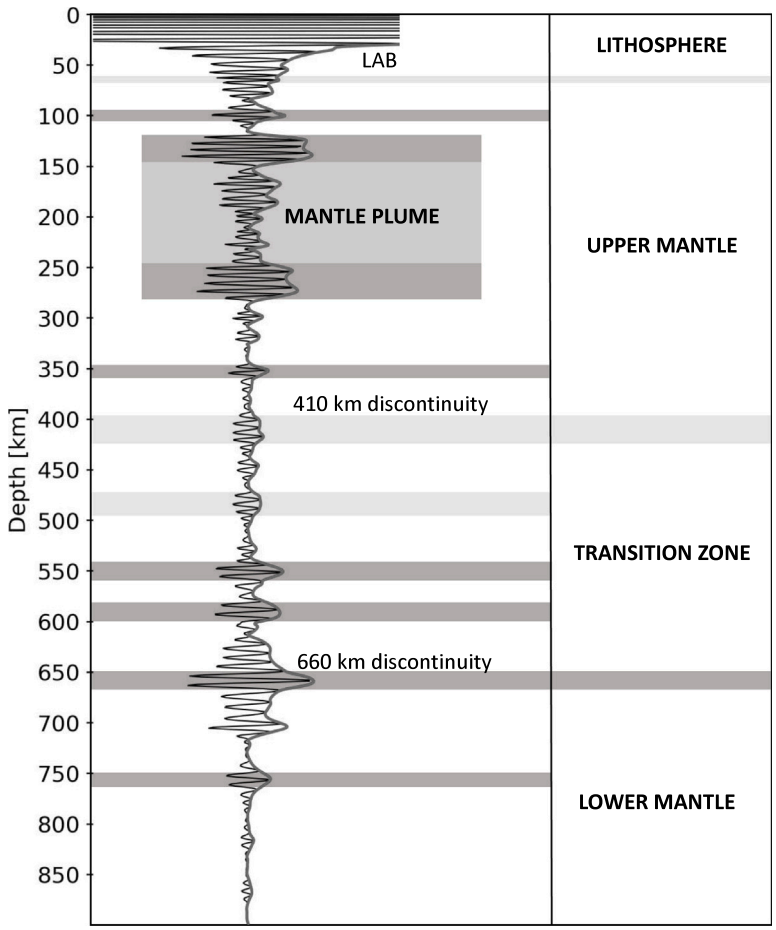

Fig. 7. Resulting reflection trace and subsurface model. Dark-gray bands indicate features in the trace interpreted as subsurface reflectors. Light-gray bands indicate discontinuities reported in previous studies, which appear less prominently in our results. In all cases, the band width represents the width of the corresponding pulse in the resulting trace (see text for details).

and 318.6 km, which are closer to the expected depth of this discontinuity (310 ± 20 km, according to Deuss and Woodhouse (2002)). Therefore, we interpret all of these observations collectively as a possible partitioning of this compositional transition.

The 410 km discontinuity, marking the boundary between the upper mantle and the TZ, is globally recognized (Frost, 2008) and is expected to be present in this region. In our results, a change in relative amplitudes is observed across two pulses located around this depth range, at 404.4 ± 3.1 km and 417.4 ± 11.1 km with comparable amplitudes and frequency. These pulses are equivalent to a mean depth of 414.9 ± 13.6 km. The signal does not exhibit a clear local maximum compared to surrounding depths, making it difficult to identify without prior knowledge. For this reason, the 410 km discontinuity is represented by a light-gray band in Fig. 7.

Within the TZ, we identify two discontinuities at depths of 483.9 ± 8.8 km and 550.9 ± 6.2 km, with low and high prominence, respectively. We associate both of these features with a compositional transition, which is typically observed at a depth of approximately 520 km in other regions worldwide (Shearer, 1990). This interpretation is consistent with the findings of Deuss and Woodhouse (2001), who also describe a partitioning of this depth with peaks around 500 and 560 km for some regions of the world, including Galápagos.

Another discontinuity is observed within the TZ at 591.5±7.1 km. We associate this feature with the beginning of a low-velocity layer at the base of the TZ. This layer is related to mineral phase transformations and the accumulation of subducted oceanic crust, which can become trapped at the base of the TZ, forming a stable and dense layer approximately 50-km-thick just above the 660 km discontinuity (Ringwood, 1968; Shen et al., 2014).

The lower boundary of the TZ, marking the beginning of the lower mantle, is observed at a depth of 659 ± 8.6 km, consistent with global observations (Shearer, 1990). The corresponding pulse maximum at 659 km, shown in Fig. 6, is clear and well-defined, but surrounded by relatively high amplitudes, spanning approximately from 620 to an estimated 700 km. This broadening may reflect structural or compositional complexity at the base of the TZ. A smaller secondary peak appears near 720.9 km; we infer that this feature likely originates from constructive interference between the broad 659 km pulse and a structural heterogeneity within the same discontinuity. This is followed by an additional reflector at 756.1 ± 6.52 km. The complexity of this region has also been documented in previous studies; Deuss (2009) reported evidence of multiple reflectors and highlighted the heterogeneous nature of the transition from the TZ to the lower mantle, including the possible presence of double peaks near 650 and 750 km in some regions of the world.

In this study, we limit the analysis to the first 200 s of the P-wave coda, selecting this time window to ensure contributions from all events at each station. This approach allows imaging of structures down to approximately 900 km depth. Although deeper discontinuities are not addressed in this work, alternative strategies such as considering only long P-wave codas or assigning weights according to the length of the codas could be implemented in future studies to reveal deeper features.

This work represents the first application of SI to image mantle discontinuities at such depths beneath the Galápagos. For this analyzed depth range, we provide coherent and robust results that enhance our understanding of the regional mantle structures. These insights may have significant implications for future studies on magma evolution

(e.g., Galetto et al. (2023)) and, consequently, for hazard assessment approaches (Hidalgo et al., 2023).

6. Conclusions

We applied seismic interferometry by autocorrelation to seismic events recorded at 18 temporary stations located in the southern part of Isabela Island (Western Galápagos) for retrieval of body-wave reflections. For each of the stations, we selected seismic events based on their magnitude and epicentral distance to ensure vertical incidence of P-wave energy. This approach allowed us to retrieve virtual sources co-located with the recording stations on the surface, which we subsequently summed together to obtain one final virtual zero-offset trace to interpret as representative of the subsurface below the 18 stations. Our results indicate the depth of discontinuities in the subsurface below the stations, which are in accordance with those expected for the area. While most identified features are robust and well resolved, a limited subset remains tentative. These tentative discontinuities correspond to the lithosphere asthenosphere boundary at ~65 km, the upper mantle transition zone boundary at ~415 km, and the upper interface of the 520 km discontinuity at ~484 km. All remaining discontinuities are robust. These include features associated with compositional or mineralogical transitions within the upper mantle at ~100 km and ~352 km; the second interface of the 520 km discontinuity at ~551 km; the onset of a low-velocity layer at ~591 km; and the transition zone lower mantle boundary at ~659 km, with a second reflector at ~756 km. Furthermore, we evidenced the upper and lower boundaries of the Galápagos mantle plume within the upper mantle at ~138 km and ~270 km, respectively. This supports a tilted and deflected geometry of the mantle plume beneath the archipelago. While some of the utilized events exhibited seemingly low signal-to-noise ratios probably caused by the complex geological environment of the Galápagos, the results support that seismic interferometry for body-wave retrieval can still be effectively applied in such conditions. By implementing rigorous quality control, frequency filtering, and a two-stage stacking process, we were able to enhance the signal coherence and improve the overall quality of the final results. This underscores the robustness of the seismic interferometry by autocorrelation technique in extracting coherent structural information. This study represents the first application of seismic interferometry for body-wave retrieval to image mantle discontinuities beneath the Galápagos. This approach enabled a more detailed characterization of discontinuities at various depths, providing evidence that supports the notion of structural complexity in some of these interfaces. We expect that our findings on mantle structures will contribute to a better characterization of the Galápagos hotspot, its linkage to the Galápagos Spreading Center, and the volcanic activity of the region.

Research data

This study was conducted using openly available seismic data from the SIGNET network, retrieved from the Incorporated Research Institutions for Seismology (IRIS) Data Management Center (https://doi.org/10.7914/SN/XE_2009). We used the open-source software PyWEED (developed by IRIS, https://github.com/iris-edu/pyweed) for data selection and download. We processed the data using Python and its scientific libraries, highlighting the use of the ObsPy library (https://doi.org/10.1785/gssrl.81.3.530). Map figures were generated using the Generic Mapping Tools (GMT, https://www.generic-mapping-tools.org/).

CRediT authorship contribution statement

Eugenia Boero: Writing – review & editing, Writing – original draft, Visualization, Software, Formal analysis, Data curation. **José Augusto Casas:** Writing – review & editing, Methodology, Conceptualization. **Gabriela Alejandra Badi:** Writing – review & editing, Supervision, Conceptualization. **Deyan Draganov:** Writing – review & editing, Supervision, Conceptualization.

Declaration of competing interest

The authors declare that they have no known competing financial interests or personal relationships that could have appeared to influence the work reported in this paper.

Appendix A. Frequency-range selection

We conducted a frequency-spectrum analysis of the noise and the P-wave coda intervals of the events in order to identify a frequency range in which, for all events, the energy of the signal consistently exceeds that of the noise, even though the signal-to-noise ratio (SNR) varies across events.

To illustrate this analysis, we select two representative events with different SNRs, both recorded at the same station (GS17). One event, with an epicentral distance of 37.38° and a magnitude of M_w 7, shows a high SNR. In Fig. A.1(a), the vertical component of the record is shown, along with the arrivals of the P and S phases, and the windows corresponding to noise and the P-wave coda. The considered P-wave coda window is 200-s-long, as this is the segment later used for signal processing. In this case, a comparison of the frequency spectra of the noise and the P-wave coda (Fig. A.1(b)) shows that the energy of the P-wave exceeds that of the noise between approximately 0.1 and 11 Hz.

The second event, with a magnitude of M_w 6.3 and an epicentral distance of 76.08° (Fig. A.2(a)), exhibits a lower SNR. As in the previous case, the trace shows the P and S arrivals and the selected windows for noise and P-wave coda. Here as well, the P-wave coda window is 200-s-long. Fig. A.2(b) shows a noticeable amplitude difference between signal and noise in the [0.5, 1] Hz range, although it is much less pronounced than for the first event. At other frequencies, the energy levels of the noise and the P-wave are similar in magnitude. Despite the differences in SNR, the energy of the signal is sufficiently high compared to that of noise for a frequency range of [0.5, 1] Hz.

Appendix B. Stability of the single-station linear stack

We evaluated the stability of the linear stacking procedure at the single-station level by performing a subsampling (bootstrapping) analysis of autocorrelations. To this end, we selected station GS01 as a representative example. This station comprises a total of 238 selected seismic traces, yielding 238 autocorrelation functions. All available autocorrelations were used to compute their linear stack, hereafter referred to as the reference stack.

To assess the stability of the stacked signal, we generated an ensemble of subsampled stacks by randomly selecting 60 autocorrelations from the full dataset. This procedure was repeated 60 times, yielding 60 independent subsampled linear stacks. Each realization includes less than one quarter of the available data, making this a stringent bootstrap test. Each subsampled stack, as well as the reference stack, was normalized by its maximum absolute amplitude to enable direct comparison of waveform similarity (Fig. B.1). Visual inspection indicates a high degree of similarity between the main features observed in the reference stack and those obtained from the subsampled stacks.

To quantify the differences between the subsampled stacks and the reference stack, we computed the mean absolute error (MAE) in the time domain. First, the MAE was calculated sample by sample, yielding a time-dependent error curve shown in Fig. B.2. The maximum sample-wise MAE reaches a value of 0.0145. In addition, when averaging over all time samples and all subsampled stacks, the resulting global MAE is 0.00398. The corresponding root mean square error (RMSE) is 0.00561.

The low MAE and RMSE values indicate that the linear stack is stable under random subsampling of the available autocorrelations. Given the stringent nature of this bootstrap test, in which some individual subsampled stacks may lack specific events present in the reference stack, the consistency observed across realizations provides strong evidence for the stability of the stacking procedure. Since stacking over

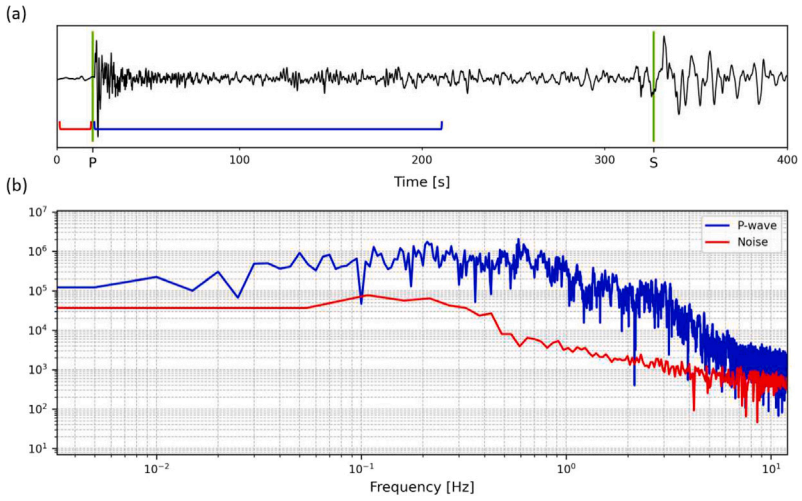

Fig. A.1. (a) The trace corresponding to the vertical component of an event that occurred in Santiago del Estero (Argentina), recorded by station GS17. Green vertical lines delineate the arrivals of the P and S phases. The blue section indicates the time window considered for extraction of the P-wave coda, while the red section highlights the noise time window utilized for spectral comparison. (b) A log–log scale plot of the amplitude spectra derived from the P-wave coda window (blue) and the noise window (red), illustrating the energy distribution across frequencies within these selected time windows.

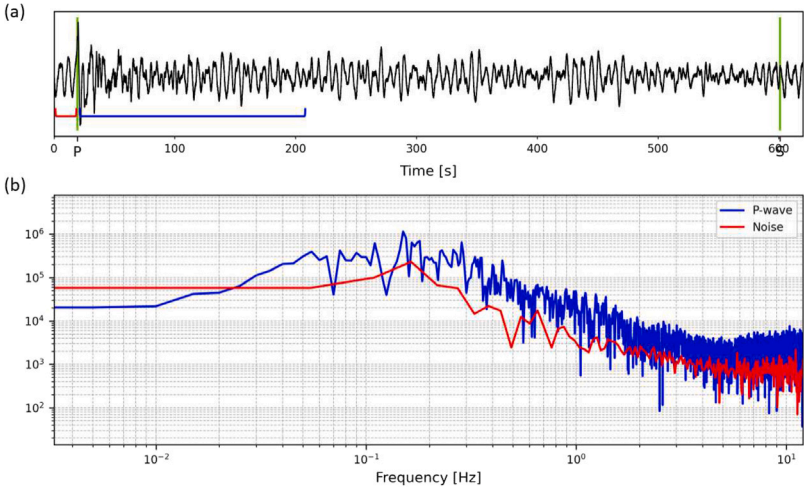

Fig. A.2. As in Fig. A.1 but an event that occurred in South Sandwich Islands.

a large number of events ensures a more complete and reliable representation of the signal, this result implies that the final stack using all available autocorrelations is particularly robust. These results further demonstrate that the stacked autocorrelation signal is not dominated by a small subset of traces, but instead reflects a coherent contribution from the dataset as a whole, yielding a waveform consistent with the reference stack solution.

Appendix C. Velocity-model sensitivity

We conducted a velocity-model sensitivity analysis to evaluate the impact of velocity uncertainties on the time-to-depth conversion of the phase-weighted stacking (PWS) resulting trace. To this end, we considered perturbations of the velocity model adopted in this study, hereafter referred to as the reference model. We generated an ensemble of 50 perturbed velocity models by randomly modifying the P-wave velocity of the reference model within ±5% at all depths. Each perturbed model was then used to convert the final PWS signal from time to depth (Fig. C.1).

We evaluated the uncertainty by computing the absolute depth deviation between the reference model and each perturbed model for every sample of the PWS. These deviations were then averaged across the ensemble of perturbed models. The resulting mean deviations for each depth, relative to the reference model, are shown in Fig. C.2.

As expected, the deviation increases with depth due to the cumulative effect of velocity uncertainties. The maximum average deviation is observed at the greatest investigated depths (> 700 km), where it reaches values of about 5.21 km. Even at these depths, the deviations remain small compared to the absolute depth scale of the investigated structures. When averaging over all samples and all perturbed models, the resulting mean absolute depth deviation is approximately 3.16 km. Given that the applied ±5% perturbation represents a relatively large velocity uncertainty, particularly for global velocity models, these results indicate that the depth conversion is only weakly affected by plausible velocity variations.

This sensitivity analysis demonstrates that the depth-domain results are robust with respect to reasonable variations in the velocity model, reinforcing the conclusion that velocity-model uncertainties do not significantly affect the interpretation of the imaged reflectors.

Appendix D. Supplementary data

Supplementary material related to this article can be found online at https://doi.org/10.1016/j.pepi.2026.107556.

Fig. B.1. Reference linear stack computed using all available autocorrelations (black), compared with subsampled linear stacks obtained from random subsets of autocorrelations (colored).

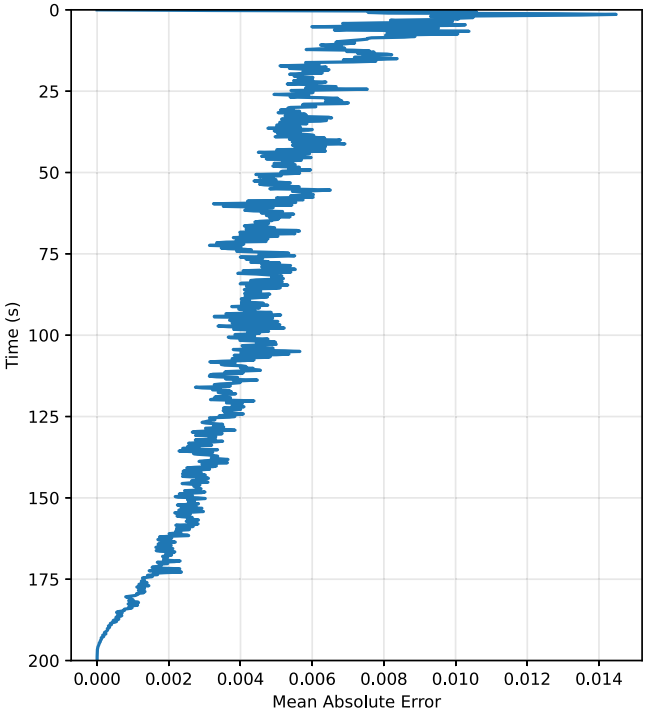

Fig. B.2. Sample-by-sample mean absolute error (MAE) between the subsampled linear stacks and the reference stack for station GS01.

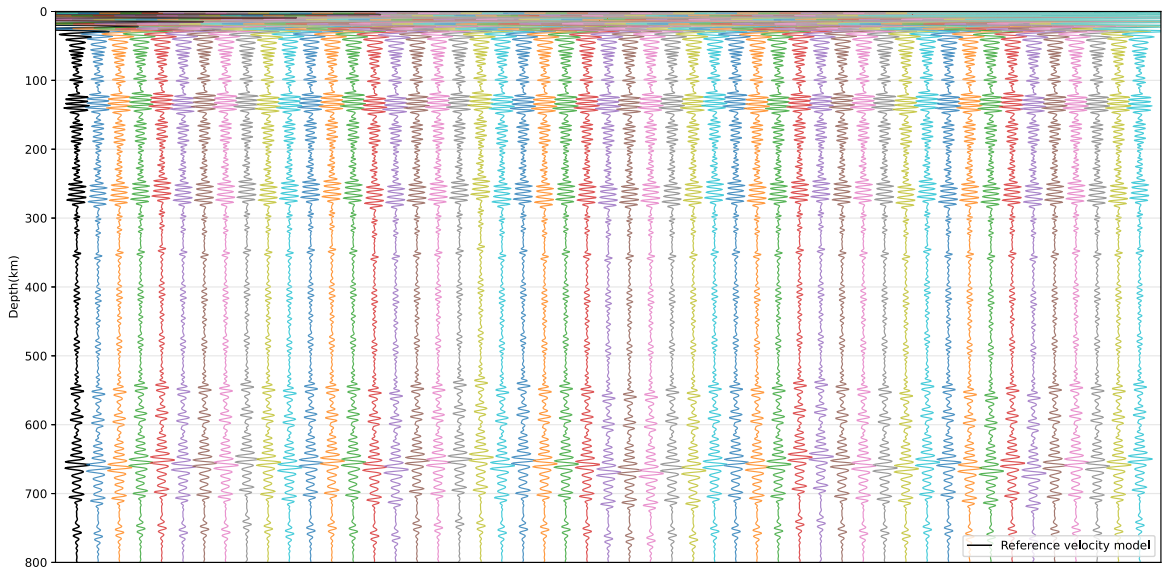

Fig. C.1. Final PWS converted from time to depth using the reference velocity model (black) and perturbed velocity models (colored).

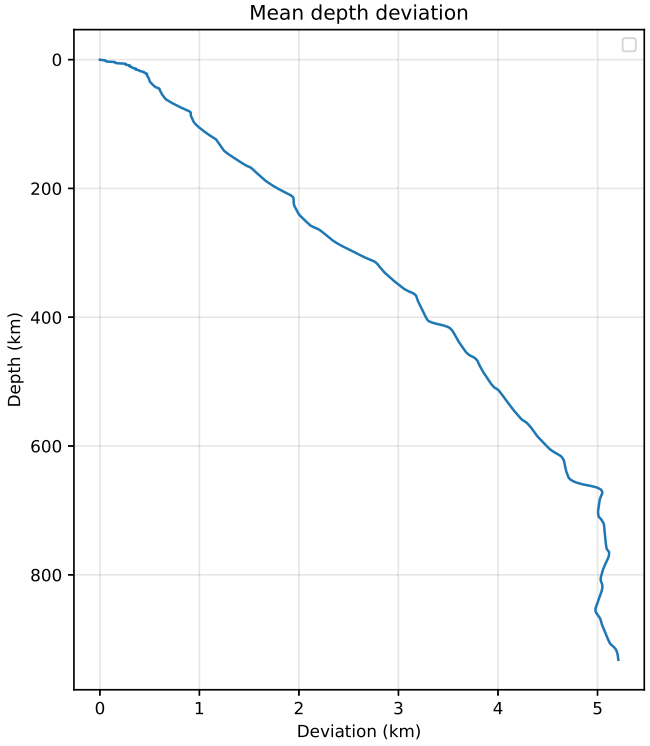

Fig. C.2. Mean absolute depth deviation relative to the reference velocity model, computed from the ensemble of perturbed models.

Data availability

Seismic waveform data from the SIGNET network (Original data) (Incorporated Research Institutions for Seismology (IRIS))

References

Boullenger, B., Verdel, A., Paap, B., Thorbecke, J., Draganov, D., 2014. Studying CO_2 storage with ambient-noise seismic interferometry: A combined numerical feasibility study and field-data example for ketzin, Germany. Geophysics 80, Q1–Q13. http://dx.doi.org/10.1190/geo2014-0181.1.

Brenguier, F., Campillo, M., Hadziioannou, C., Shapiro, N.M., Nadeau, R.M., Larose, E., 2008. Postseismic relaxation along the san andreas fault at parkfield from continuous seismological observations. Science 321 (5895), 1478–1481. http://dx.doi.org/10.1126/science.1160943.

Byrnes, J., Hooft, E., Toomey, D., Villagomez, D., Geist, D., Solomon, S., 2015. An upper-mantle seismic discontinuity beneath the galápagos archipelago and its implications for studies of the lithosphere-asthenosphere boundary. Geochem. Geophys. Geosystems 16, http://dx.doi.org/10.1002/2014GC005694.

Casas, J., Badi, G., Franco-Marín, L.E., Draganov, D., 2020. Seismic interferometry applied to regional and teleseismic events recorded at planchón-peteroa volcanic complex, Argentina-Chile. J. Volcanol. Geotherm. Res. 393, 106805. http://dx.doi.org/10.1016/j.jvolgeores.2020.106805.

Casas, J., Draganov, D., Badi, G., Manassero, C., Olivera Craig, V., Franco-Marín, L.E., Gómez, M., Ruigrok, E., 2019. Seismic interferometry applied to local fracture seismicity recorded at planchón-peteroa volcanic complex, Argentina-Chile. J. South Am. Earth Sci. 92, 134–144. http://dx.doi.org/10.1016/j.jsames.2019.03.012.

Claerbout, J., 1968. Synthesis of a layered medium from its acoustic transmission response. Geophysics 33, 264–269. http://dx.doi.org/10.1190/1.1439927.

Delph, J., Levander, A., Niu, F., 2019. Constraining crustal properties using receiver functions and the autocorrelation of earthquake-generated body waves. J. Geophys. Res.: Solid Earth 124, 8981–8997. http://dx.doi.org/10.1029/2019JB017929.

Deuss, A., 2009. Global observations of mantle discontinuities using SS and PP precursors. Surv. Geophys. 30, 301–326. http://dx.doi.org/10.1007/s10712-009-9078-y.

Deuss, A., Woodhouse, J., 2001. Seismic observations of splitting of the mid-transition zone discontinuity in earth's mantle. Sci. (New York, N.Y.) 294, 354–357.. http://dx.doi.org/10.1126/science.1063524.

Deuss, A., Woodhouse, J., 2002. A systematic search for mantle discontinuities using SS-precursors. Geophys. Res. Lett. - GEOPHYS RES LETT 29, 90–1 – 90–4. http://dx.doi.org/10.1029/2002GL014768.

Draganov, D., Wapenaar, K., Mulder, W., Singer, J., Verdel, A., 2007. Retreival of reflections from background-noise measurements. Geophys. Res. Lett. 34, L04305+. http://dx.doi.org/10.1029/2006GL028735.

Frost, D., 2008. The upper mantle and transition zone. Elements 4, 171–176. http://dx.doi.org/10.2113/GSELEMENTS.4.3.171.

Galetto, F., Reale, D., Sansosti, E., Acocella, V., 2023. Implications for shallow magma transfer during the 2017 and 2018 eruptions at fernandina (galápagos) inferred from InSAR data. J. Geophys. Res.: Solid Earth 128, http://dx.doi.org/10.1029/2022JB026174.

Geist, D., Bergantz, G., Chadwick, W., 2014. Galápagos magma chambers. Geophys. Monogr. Ser. 55–69. http://dx.doi.org/10.1002/9781118852538.ch5.

Geist, D., Harpp, K., Naumann, T., Poland, M., Chadwick, W., Hall, M.L., Rader, E., 2008. The 2005 eruption of sierra negra volcano, galápagos, ecuador. Bull. Volcanol. 70, 655–673. http://dx.doi.org/10.1007/s00445-007-0160-3.

Geist, D., White, W., McBirney, A., 1988. Plume-asthenosphere mixing beneath the galápagos archipelago. Nature 333, http://dx.doi.org/10.1038/333657a0.

Gorbatov, A., Saygin, E., Kennett, B., 2013. Crustal properties from seismic station autocorrelograms. Geophys. J. Int. 192, 861–870. http://dx.doi.org/10.1093/gji/ggs064.

Harpp, K., Geist, D., 2018. The evolution of galápagos volcanoes: An alternative perspective. Front. Earth Sci. 6, 50. http://dx.doi.org/10.3389/feart.2018.00050.

Hassing, S., Draganov, D., Janssen, M., Barnhoorn, A., Wolf, K.H., Berg, J., Friebel, M., Otten, G., Poletto, F., Bellezza, C., Barison, E., Brynjarsson, B., Hjörleifsdóttir, V., Obermann, A., Sánchez-Pastor, P., Durucan, S., 2023. Imaging CO reinjection into basalts at the CarbFix2 reinjection reservoir (hellisheii, iceland) with body-wave seismic interferometry. Geophys. Prospect. 72, http://dx.doi.org/10.1111/1365-2478.13472.

Heath, B., Hooft, E., Toomey, D., 2018. Autocorrelation of the seismic wavefield at newberry volcano: Reflections from the magmatic and geothermal systems. Geophys. Res. Lett. 45, http://dx.doi.org/10.1002/2017GL076706.

Hey, R., 1977. Tectonic evolution of the cocos-nazca spreading center. Geol. Soc. Am. Bull. - GEOL SOC AMER BULL 88, 1404–1420. http://dx.doi.org/10.1130/0016-7606(1977)88<1404:TEOTCS>2.0.CO;2.

Hidalgo, S., Bernard, B., Mothes, P., Ramos, C., Aguilar, J., Andrade, D., Samaniego, P., Yepes, H., Hall, M.L., Alvarado, A., Segovia, M., Ruiz Fernandez, M., Ramon, P., Vaca, M., 2023. Hazard assessment and monitoring of ecuadorian volcanoes: challenges and progresses during four decades since IG-EPN foundation. Bull. Volcanol. 86, http://dx.doi.org/10.1007/s00445-023-01685-6.

IRIS, 2015. PyWEED. Cross-platform application for retrieving event-based seismic data. URL https://github.com/iris-edu/pyweed.

Kennett, B., Engdahl, E., Buland, R., 1995. Constraints on seismic velocities in the earth from travel-times. Geophys. J. Int. 122, 108–124. http://dx.doi.org/10.1111/j.1365-246X.1995.tb03540.x.

Kim, D., Brown, L., Árnason, K., Ágústsson, K., Blanck, H., 2017. Magma reflection imaging in krafla, iceland, using microearthquake sources: Magma imaging with microearthquakes. J. Geophys. Res.: Solid Earth 122, 5228–5242. http://dx.doi.org/10.1002/2016JB013809.

Leven, J., 1985. The application of synthetic seismograms to the interpretation of the upper mantle P-wave velocity structure in northern Australia. Phys. Earth Planet. Inter. 38, 9–27. http://dx.doi.org/10.1016/0031-9201(85)90119-0.

Li, X., Kind, R., Yuan, X., Woelbern, I., Hanka, W., 2004. Rejuvenation of the lithosphere by the hawaiian plume. Nature 427, 827–829. http://dx.doi.org/10.1038/nature02349.

Montelli, R., Nolet, G., Dahlen, F., Masters, G., Engdahl, E., Hung, S.H., 2004. Finite-frequency tomography reveals a variety of plumes in the mantle. Sci. (New York, N.Y.) 303, 338–343. http://dx.doi.org/10.1126/science.1092485.

Nacif, S., Schimmel, M., Nacif, A., Laura, G., Lupari, M., Furlani, R., Gimenez, M., Folguera, A., 2024. Insights into the crustal and the magmatic feeding structure at the payunia volcanic province highlighted by geophysical methods, in the retroarc of the southern central andes. J. Geodyn. 162, 102059. http://dx.doi.org/10.1016/j.jog.2024.102059.

Nishitsuji, Y., Ruigrok, E., Gómez, M., Wapenaar, K., Draganov, D., 2016. Reflection imaging of aseismic zones of the nazca slab by global-phase seismic interferometry. Interpretation 4, SJ1–SJ16. http://dx.doi.org/10.1190/INT-2015-0225.1.

Oren, C., Nowack, R., 2017. Seismic body-wave interferometry using noise autocorrelations for crustal structure. Geophys. J. Int. 208, 321–332. http://dx.doi.org/10.1093/gji/ggw394.

Pham, T.S., Tkalčić, H., 2017. On the feasibility and use of teleseismic P- wave coda autocorrelation for mapping shallow seismic discontinuities. J. Geophys. Res.: Solid Earth 122, http://dx.doi.org/10.1002/2017JB013975.

Polychronopoulou, K., Lois, A., Draganov, D., 2019. Body-wave passive seismic interferometry revisited: Mining exploration using the body waves of local microearthquakes. Geophys. Prospect. 68, http://dx.doi.org/10.1111/1365-2478.12884.

Ringwood, A., 1968. Phase transformations in mantle. Earth Planet. Sci. Lett. 5, 401–412. http://dx.doi.org/10.1016/S0012-821X(68)80072-X.

Ruigrok, E., Campman, X., Draganov, D., Wapenaar, K., 2010. High-resolution lithospheric imaging with seismic interferometry. Geophys. J. Int. 183, 339–357. http://dx.doi.org/10.1111/j.1365-246X.2010.04724.x.

Ruigrok, E., Wapenaar, K., 2012. Global-phase seismic interferometry unveils P-wave reflectivity below the himalayas and tibet. Geophys. Res. Lett. 39, 11303. http://dx.doi.org/10.1029/2012GL051672.

Rychert, C., Harmon, N., Ebinger, C., 2014. Receiver function imaging of lithospheric structure and the onset of melting beneath the galápagos archipelago. Earth Planet. Sci. Lett. 388, 156–165. http://dx.doi.org/10.1016/j.epsl.2013.11.027.

Sens-Schönfelder, C., Wegler, U., 2006. Passive image interferometry and seasonal variations of seismic velocities at merapi volcano, Indonesia. Geophys. Res. Lett. 33 (21), L21302. http://dx.doi.org/10.1029/2006GL027797.

Shearer, P., 1990. Seismic imaging of upper-mantle structure with new evidence for a 520-km discontinuity. Nature 344, 121–126. http://dx.doi.org/10.1038/344121a0.

Shen, X., Yuan, X., Li, X., 2014. A ubiquitous low velocity layer at the base of the mantle transition zone. Geophys. Res. Lett. 41, http://dx.doi.org/10.1002/2013GL058918.

Siebert, L., Simkin, T., Kimberly, P., 2010. Volcanoes of the World: Third Edition, third ed. University of California Press, p. 568, URL http://www.jstor.org/stable/10.1525/j.ctt1pnqdx.

Sigurdsson, H., Houghton, B., McNutt, S., Rymer, H., Stix, J. (Eds.), 2015. The Encyclopedia of Volcanoes, second ed. Academic Press, Amsterdam.

Simkin, T., 1984. Geology of galapagos. Biol. J. Linnean Soc. 21 (1–2), 61–75. http://dx.doi.org/10.1111/j.1095-8312.1984.tb02053.x.

Simkin, T., Howard, K.A., 1970. Caldera collapse in the galápagos islands, 1968. Science 169 (3944), 429–437. http://dx.doi.org/10.1126/science.169.3944.429.

Sun, W., Kennett, B., 2016. Receiver structure from teleseisms: auto- and cross-correlation: SEISMIC DAYLIGHT IMAGING. Geophys. Res. Lett. 43, http://dx.doi.org/10.1002/2016GL069564.

Tauzin, B., Pham, T.S., Tkalčić, H., 2019. Receiver functions from seismic interferometry: A practical guide. Geophys. J. Int. 1–25. http://dx.doi.org/10.1093/gji/ggz002.

Vasconcelos, I., Snieder, R., Douma, H., 2009. Representation theorems and green's function retrieval for scattering in acoustic media. Phys. Rev. E, Stat. Nonlinear Soft Matter Phys. 80, 036605. http://dx.doi.org/10.1103/PhysRevE.80.036605.

Ventosa, S., Schimmel, M., 2017. Extracting surface waves, hum and normal modes: Time-scale phase-weighted stack and beyond. Geophys. J. Int. 211, 30–44. http://dx.doi.org/10.1093/gji/ggx284.

Villagómez, D., Toomey, D., Geist, D., Hooft, E., Solomon, S., 2014. Mantle flow and multistage melting beneath the galápagos hotspot revealed by seismic imaging. Nat. Geosci. 7, 151–156. http://dx.doi.org/10.1038/ngeo2062.

Wajeman, N., 1988. Detection of underside P-reflections at mantle discontinuities by stacking broad-band data. Geophys. Res. Lett. - GEOPHYS RES LETT 15, 669–672. http://dx.doi.org/10.1029/GL015i007p00669.

Wapenaar, K., Draganov, D., Snieder, R., Campman, X., Verdel, A., 2010. Tutorial on seismic interferometry. Part I: Basic principles and applications. Geophysics 75, 75A195–75209. http://dx.doi.org/10.1190/1.3457445.

Wapenaar, K., Fokkema, J., 2006. Green's function representation for seismic interferometry. Geophysics 71, SI33–SI46. http://dx.doi.org/10.1190/1.2213955.

Williams, Q., Revenaugh, J., 2005. Ancient subduction, mantle eclogite, and the 300 km seismic discontinuity. Geology 33, 1–4. http://dx.doi.org/10.1130/G20968.1.

Yang, X., Bryan, J., Okubo, K., Jiang, C., Clements, T., Denolle, M., 2022. Optimal stacking of noise cross-Correlation functions. Geophys. J. Int. 232, http://dx.doi.org/10.1002/essoar.10511292.2.